

Exploring the Energetics of Intracluster Gas with a Simple and Accurate Model

Paul Bode and Jeremiah P. Ostriker

Department of Astrophysical Sciences, Peyton Hall, Princeton University, Princeton, NJ 08544; bode@astro.princeton.edu, ostriker@princeton.edu

Alexey Vikhlinin

Harvard-Smithsonian Center for Astrophysics, 60 Garden St., Cambridge, MA 02138; avikhlinin@cfa.harvard.edu

ABSTRACT

The state of the hot gas in clusters of galaxies is investigated with a set of model clusters, created by assuming a polytropic equation of state ($\Gamma = 1.2$) and hydrostatic equilibrium inside gravitational potential wells drawn from a dark matter simulation. Star formation, energy input, and nonthermal pressure support are included. To match the gas fractions seen in non-radiative hydrodynamical simulations, roughly 5% of the binding energy of the dark matter must be transferred to the gas during cluster formation; the presence of nonthermal pressure support increases this value. In order to match X-ray observations, scale-free behavior must be broken. This can be due to either variation of the efficiency of star formation with cluster mass M_{500} , or the input of additional energy proportional to the formed stellar mass M_F . These two processes have similar effects on X-ray scalings. If 9% of the gas is converted into stars, independent of cluster mass, then feedback energy input of $1.2 \times 10^{-5} M_F c^2$ (or ~ 1.0 keV per particle) is required to match observed clusters. Alternatively, if the stellar mass fraction varies as $\propto M_{500}^{-0.26}$ then a lower feedback of $4 \times 10^{-6} M_F c^2$ is needed, and if the stellar fraction varies as steeply as $\propto M_{500}^{-0.49}$ then no additional feedback is necessary. The model clusters reproduce the observed trends of gas temperature and gas mass fraction with cluster mass, as well as observed entropy and pressure profiles; thus they provide a calibrated basis with which to interpret upcoming SZ surveys. One consequence of the increased gas energy is that the baryon fraction inside the virial radius is $\lesssim 90\%$ of the cosmic mean, even for the most massive clusters.

Subject headings: cosmology:theory — galaxies:clusters:general — intergalactic medium — X-rays:galaxies:clusters

1. Introduction

In the near future, clusters of galaxies will prove to be an increasingly important probe into the abundance and properties of both dark matter and dark energy. Data on large numbers of clusters are becoming available from surveys at many wavelengths: in the optical/infrared, from galaxy overdensities (Koester et al. 2007; Yee et al. 2007; Eisenhardt et al. 2008; Lopes et al. 2009) or from weak gravitational lensing of background objects (Dahle 2007); in the X-ray (Böhringer et al. 2007; Burenin et al. 2007; Finoguenov et al. 2007; Pacaud et al. 2007); and in the microwave, by locating temperature decrements caused by the Sunyaev-Zeldovich (SZ) effect (Dobbs et al. 2006; Kosowsky 2006; Malte Schäfer & Bartelmann 2007; Muchovej et al. 2007; Lin et al. 2008; Bonamente et al. 2008; Staniszewski et al. 2008).

Properly interpreting such surveys will require a sound understanding of the state of the Intra-Cluster Medium (ICM). Based on the assumption that the thermal energy in the gas comes solely from gravitational collapse, one may derive expected self-similar scalings between halo mass and temperature, X-ray luminosity, etc. (Kaiser 1991; Bryan & Norman 1998; Eke et al. 1998). However, these scalings do not match the actual behavior of observed clusters (e.g. Arnaud & Evrard 1999; Vikhlinin et al. 2006; Arnaud et al. 2007; Pratt et al. 2008; Sun et al. 2009; Vikhlinin et al. 2009). Additional modification of the thermal state of the gas from non-gravitational sources will bring these predictions into better agreement with observed scalings (Kaiser 1991). One such modification is star formation; by removing gas with the shortest cooling times, star formation leaves behind gas with a higher mean entropy (Voit & Bryan 2001; Tozzi & Norman 2001; Voit et al. 2002). Energy injection from preheating or stellar and AGN feedback likewise affects scalings, as numerous simulations which include such feedback have shown (e.g. Ettori et al. 2006; Borgani et al. 2006; Muanwong et al. 2006; Nagai et al. 2007; Kay et al. 2007; Sijacki et al. 2007; Bhattacharya et al. 2008; Borgani et al. 2008; Davé et al. 2008; Puchwein et al. 2008; Short & Thomas 2008, and references therein). The importance of these processes can be investigated analytically by considering hydrostatic, and usually polytropic, gas residing in various dark matter potentials (Suto et al. 1998; Balogh et al. 1999; Wu et al. 2000; Loewenstein 2000; Tozzi & Norman 2001; Komatsu & Seljak 2001; Babul et al. 2002; Voit et al. 2002; Dos Santos & Doré 2002; Ascasibar et al. 2003; Shimizu et al. 2004; Lapi et al. 2005; Afshordi et al. 2005; Solanes et al. 2005; Ascasibar & Diego 2008; Bower et al. 2008; Ciotti & Pellegrini 2008; Moodley et al. 2008).

Ostriker et al. (2005, hereafter Paper I) and Bode et al. (2007, Paper II) developed a simple method for populating the halo Dark Matter (DM) potentials from N-body simulations with gas, based on the assumptions of hydrostatic equilibrium and a polytropic equation of state. This method can be calibrated against local X-ray observations, and then be used to create realistic sky maps (Sehgal et al. 2007). Rather than assuming a simple analytic

profile, the distributions of halo concentration, substructure, and triaxiality are included, as well as any spatial correlations, since the halos are drawn from an accurate large scale dark matter simulation. This procedure has advantages over performing full hydrodynamic simulations. Because less computational expense is required, large volumes can be simulated. Also, one can vary parameters, such as the amount of star formation and feedback, without having to redo an entire simulation.

This paper presents a number of improvements to the model presented in Paper I and Paper II. A more sophisticated description of star formation is included, which accounts for gas recycling and allows for a calculation of metallicity evolution. Paper II assumed that every cluster halo has the same stellar mass fraction; here we allow this fraction to vary with halo mass. Also Paper II did not allow for transfers of energy from the dark matter to the gas. It is evident from simulations that this does occur, so we allow for this transfer here. Because of these limitations, Paper II required a large amount of feedback energy to match X-ray observations. As we shall see, the improvements presented here significantly reduce the feedback required.

With this method, we examine how star formation and different forms of energy input affect the ICM. It is possible to produce model clusters which match existing observational constraints, and thus make predictions for upcoming surveys. The method is described in Sec. 2 and Appendix A. In Sec. 3 it is then applied to a simulation reflecting the current best-fit cosmological parameters and the results are compared to X-ray data; in particular the effects of varying star formation and feedback are examined. In Sec. 4 a standard model is compared to further X-ray and SZ observation; we summarize and discuss implications in Sec. 5.

2. Method

To create a mock catalog, cluster-sized halos are extracted from a dark matter only N-body simulation, and then the gas distribution inside each halo potential is determined. This section describes the gas model and the construction of the halo catalog which is used.

2.1. The Gas Prescription

A given DM halo is enclosed in a cubic mesh, using a cell size, l , twice the N-body particle spline softening length. The DM density, ρ_{Dk} , and gravitational potential, ϕ_k , are computed for each cell k using a Particle-Mesh code with non-periodic boundary conditions.

The cell with the lowest potential, $\phi_0 = \text{MIN}(\phi_k)$, is considered the center of the cluster. Particle velocities in the rest frame of the cluster (defined as the mean velocity of the 125 particles closest to the cluster center) are used to find the KE per unit volume, $\frac{1}{2}t_{Dk}$, in each cell. The virial radius (from spherical top-hat collapse; Bryan & Norman 1998) can then be computed, as well as the halo virial mass, M_D , and energy, E_D .

It is assumed that gas originally followed the DM inside the virial radius, with density $f_c\rho_{Dk}$ and KE $f_c\frac{1}{2}t_{Dk}$, where $f_c \equiv \Omega_b/\Omega_m$. A certain amount of the gas, M_* , will have turned into stars. We parameterize this mass by the fraction $f_* \equiv M_*/(f_c M_D)$ at $z=0$; the evolution of M_* with redshift is described in Appendix A. This stellar mass presumably formed from the portion of the gas with the lowest entropy and shortest cooling time, so cells are ranked by binding energy and then are checked off, starting with the most bound, until the sum of their gas masses equals M_* ; the gas mass and energy in these cells are set to zero. Thus the initial mass M_g and energy E_g of the remaining gas are:

$$M_g = \sum_k f_c \rho_{Dk} l^3 \quad , \quad (1)$$

$$E_g = \sum_k f_c \left\{ \phi_k \rho_{Dk} + \frac{1}{2} t_{Dk} \right\} l^3 \quad , \quad (2)$$

summing over all cells inside r_{vir} except those marked off for star formation. The surface pressure P_s on the gas at the virial radius is estimated from the kinetic energy in a buffer region eleven cells thick:

$$P_s = \frac{1}{3} N_b^{-1} \sum_{k=1}^{N_b} f_c t_{Dk} \quad , \quad (3)$$

summing over the N_b cells in the buffer region $r_{vir} < r_k < r_{vir} + 11l$.

From this initial state, it is assumed the gas is rearranges itself into hydrostatic equilibrium in the DM potential, with a polytropic equation of state of index $\Gamma = 1.2$ (as indicated by both observation and simulation; Paper I). The resulting gas pressure P and density ρ are given by $P_k = P_0 \theta_k^{\frac{\Gamma}{\Gamma-1}}$ and $\rho_k = \rho_0 \theta_k^{\frac{1}{\Gamma-1}}$, where the polytropic variable

$$\theta_k \equiv 1 + \frac{\Gamma - 1}{\Gamma(1 + \delta_{rel})} \frac{\rho_0}{P_0} (\phi_0 - \phi_k) \quad . \quad (4)$$

Here δ_{rel} is a nonthermal component of pressure, assumed to be everywhere proportional to thermal pressure; the total is thus $P_{tot} = (1 + \delta_{rel})P$. The pressure P_0 and density ρ_0 at the cluster center are found using two constraints: requiring conservation of energy, and matching the external surface pressure. For a given P_0 and ρ_0 , the final radius r_f of the gas initially inside r_{vir} is found by summing outwards from the cluster center until the initial mass M_g is

enclosed. Note this means that gas may expand or contract, changing the gas fraction inside r_{vir} , and also doing mechanical work. Assuming surface pressure changes little with radius, the change in energy is proportional to the change in volume: $\Delta E_p = (4\pi/3)(r_{vir}^3 - r_f^3)P_s$. The constraint equation for conservation of energy is thus (see Paper II):

$$E_f = \sum_{r_k < r_f} \left\{ \rho_0 \theta_k^{\frac{1}{\Gamma-1}} \phi_k + \frac{3}{2}(1 + 2\delta_{rel})P_0 \theta_k^{\frac{\Gamma}{\Gamma-1}} \right\} l^3 = E_g + \Delta E_P + \epsilon_D |E_D| + \epsilon_F M_F c^2 \quad . \quad (5)$$

Here there are two additional inputs to the energy budget. The penultimate term represents energy input to the gas from dynamical processes, assumed to be proportional to E_D ; the final term represents feedback energy from collapsed objects, taken to be proportional to the mass of formed stars, M_F (different from M_* once gas recycling is taken into account— see Appendix A). These additional energy inputs will be described in Sec. 3. Finally, requiring the final surface pressure to match the external pressure yields the second constraint

$$(1 + \delta_{rel})N_{rf}^{-1} \sum_{k=1}^{N_{rf}} P_0 \theta_k^{\frac{\Gamma}{\Gamma-1}} = P_s \quad , \quad (6)$$

summing over the N_{rf} bins in the radial range $r_f < r < r_f + l$. (This is a change from Paper II, which used a wider zone, thereby giving a lower measurement of surface pressure).

2.2. Creating the model cluster catalog

The gas prescription was applied to clusters selected from a large-scale N-body simulation. We will refer the reader to Paper II and Sehgal et al. (2007) for further details, as the numerical methods used to carry out this simulation are the same as described in those papers. The cosmological parameters were chosen to be $(\Omega_b, \Omega_m, \Omega_\Lambda, h, n_s, \sigma_8) = (0.044, 0.264, 0.736, 0.71, 0.96, 0.80)$, consistent with the WMAP 5-year results (Komatsu et al. 2008). The simulation volume is $1000h^{-1}\text{Mpc}$ on a side and contains $N=1024^3$ particles, making the particle mass $6.8 \times 10^{10}h^{-1}M_\odot$; the particle spline softening length is $16.3h^{-1}\text{kpc}$. At each simulation step particles were saved in one octant of a thin spherical shell centered on the origin, thus building up the matter distribution in a past light cone covering one eighth of the sky. All halos with a friends-of-friends mass of at least $2 \times 10^{13}h^{-1}M_\odot$ (293 particles) were selected from this light cone, out to redshift $z = 0.2$. Masses and radii at the virial and other overdensities are computed, in particular M_{500} and r_{500} at a mean overdensity of 500 times critical. The amount of star formation and iron production is determined based on the cluster redshift, as described in Appendix A. The gas prescription was then run on each halo; there are over 15,000 halos in this catalog with $M_{500} > 10^{13}h^{-1}M_\odot$.

To test that resolution is sufficient, a smaller sample of halos was selected from a higher resolution simulation. This has the same cosmological parameters, but the volume is $320h^{-1}\text{Mpc}$ on a side, and the softening length is $3.2h^{-1}\text{kpc}$; thus mass resolution is increased by a factor of 30.5, and spatial resolution by a factor of 5. No significant difference was seen when comparing results for lower mass halos ($M_{500} \sim 1 - 3 \times 10^{13}h^{-1}M_{\odot}$) at the two resolutions; halos more massive than this are difficult to deal with at the higher resolution because of the large grid required.

Once the density, temperature, and metallicity in each cell are known, the X-ray luminosity in the 0.5–2 keV band is computed with the MEKAL model (Mewe et al. 1985). For the cluster temperature, the mixT code of Vikhlinin (2006) was used to compute the spectroscopic temperature T_X in the projected annulus $[0.15 - 1]R_{500}$; this is the definition of cluster temperature used throughout this paper.

There are a number of parameters which must be specified: $f_*(M_{vir})$, ϵ_F , ϵ_D , and δ_{rel} . We will calibrate the model by comparing to X-ray data, in particular by matching the gas fraction as a function of T_X . Two subsamples from are selected from the halo catalog to match the properties of the two data sets we use for the calibration (this data is shown as a function of M_{500} in Figs. 1 and 2). The first data set is from Vikhlinin et al. (2006), which consists mostly of higher T_X clusters; so, for comparison, we select all halos with $M_{500} > 3 \times 10^{14}M_{\odot}$ in the $z \leq 0.2$ light cone. There are 76 halos in this subsample, with temperatures above 4 keV for most parameter choices. For a given model, we compute a $\chi_V^2 = \sum [f_g(model) - f_g(obs)]^2 / \sigma^2(obs)$, summing for each observed cluster over all model points having a T_X within 4σ of the observed T_X . The second observational set is of low redshift groups ($T_X \sim 1 - 2\text{keV}$) from Sun et al. (2009); so, for the second subsample, we select all model halos with $z < 0.0485$ and $M_{500} > 3 \times 10^{13}M_{\odot}$. This subsample also contains 76 halos, most with $T_X < 3\text{keV}$. A χ_S^2 is computed from this sample in an analogous manner as above. When searching for a best fit model we will minimize $\chi^2 = \chi_V^2 + 0.5\chi_S^2$; the factor of 0.5 ensures that the two terms contribute roughly equally near the minimum value.

3. The Role of Feedback and Star Formation

It is instructive to first consider the case of no star formation or energy input, i.e. $\epsilon_D = f_* = \epsilon_F = 0$; we will refer to this as the “Zero” model. The resulting temperature and L_X are shown as a function of mass as dotted lines in Fig. 4. Vikhlinin et al. (2009) found the $M - T_X$ relation is well fit by a power law, $E(z)M_{500} = M_0(kT/5\text{keV})^\alpha$, with $M_0 = (3.02 \pm 0.11) \times 10^{14}h^{-1}M_{\odot}$ and $\alpha = 1.53$. Fig. 1 shows the fractional difference $(T_X - T_X(obs))/T_X(obs)$, where $T_X(obs)$ is the value obtained by plugging M_{500} into the observed

relation. This figure shows that at a given M_{500} , the predicted temperature from this simple model is lower than observed, by over 10%. At the same time, it shows that the predicted gas fraction remains near the cosmic mean, and is independent of mass (quite different from what is observed). This results in a $Y_X \equiv kT_X M_g(r_{500})$ which is too high (by $\sim 20\%$ at higher masses) and an $M_{500}-Y_X$ relation with a slope near the self-similar value $Y_X \propto M_{500}^{5/3}$, slightly shallower than observed. Thus we see the simplest set of assumptions yields an incorrect gas energy. There are three main processes which can alter this energy: transfer of energy from the DM through gravitational interactions, star formation, and feedback from astrophysical sources. In this section we will consider each of these in turn.

So far (as in Paper II), it has been assumed that the gas originally had the same specific energy as the DM. However, this ignores an important process during cluster formation: when mergers occur, energy is transferred from the DM to the gas. In fact, the DM can lose up to 10% of its energy in an equal mass collision, and even a 10:1 merger can reduce the DM energy by a couple of percent (McCarthy et al. 2007). Simulations show such mergers are common: Cohn & White (2005) calculate that a typical cluster will experience four 5:1 accretion events since $z \sim 2$, and Fakhouri & Ma (2008) find that the mean rate for 10:1 or larger mergers in clusters is roughly two per halo per unit redshift. The magnitude of this effect can be estimated from hydrodynamical simulations, where it has long been found that baryon fraction in clusters is lower than the universal value (e.g. Cen & Ostriker 1994; Eke et al. 1998; Ettori et al. 2006; Gottlöber & Yepes 2007; Stanek et al. 2009). For simulations with no star formation or radiative processes, Crain et al. (2007) find that the average baryon fraction within r_{200} is 90% of the cosmic mean at $z=0$. This result is independent of cluster mass, and at $z=1$ the typical fraction is only 2 or 3% higher. Without star formation and energy feedback, the method of Sec. 2.1 gives a mean $f_g(< r_{200}) \approx f_c$ for halos with $M_{200} \geq 10^{14} h^{-1} M_\odot$ (at low redshift, $z < 0.2$). Instead assuming that the energy transferred to the gas is 5% of the DM energy, i.e. using $\epsilon_D = 0.05$ in Eqn. 5, this fraction is reduced to $0.92f_c$. As we are using a lower σ_8 than Crain et al. (2007), a slightly higher gas fraction at $z = 0$ seems appropriate. Thus we adopt $\epsilon_D = 5\%$ for the rest of the paper.

Fig. 1, and also Fig. 2, display the change in f_g inside r_{500} after including this added energy, as short-dashed lines. While lower than before, it is still higher than observed, and still roughly independent of mass. The temperature at a given mass increases, but only slightly, so the $M - Y_X$ relation is still too high and shallow. Including a term proportional to E_D in this fashion does not change the self-similar nature of the model.

Star formation will obviously decrease the gas fraction, but it has a second effect as well: since it is the most bound, lowest entropy gas that is turned into stars, the remaining gas will have a higher specific energy than before (Voit & Bryan 2001). The simplest assumption is

to make the efficiency of star formation independent of cluster mass; Fig. 2 shows, as dot-dashed lines, a $\epsilon_D = 0.05$ model after also setting $f_*=9\%$ for all halo masses. The predicted gas fraction drops further— for massive halos, near the observed value. Note the change in f_g is more than 9%; the higher specific energy of the remaining gas is a significant effect, causing that gas to expand and further reducing the gas fraction in the inner parts of the halo. Temperatures also increase, so at higher masses the predicted Y_X values are close to those observed. However, as the method up to this point has been scale-free, the gas fraction still does not depend on mass; thus, for less massive clusters, the predicted f_g and Y_X are still too large, since the slope is still the self-similar value.

There are two ways to change the scale-free nature of the models: vary star formation efficiency with halo mass, or include feedback energy proportional to stellar mass. There is observational support for both options. Lin et al. (2003), with a sample of 27 clusters, measured the fraction of stellar mass to be larger for lower mass clusters, following $M_*(< r_{500})/M_{500} = 0.0164(M_{500}/3 \times 10^{14} M_\odot)^{-\alpha_*}$ with $\alpha_* = 0.26 \pm 0.09$. To apply this to our model, we will assume this relation also holds inside the virial radius, i.e. $M_*/M_D = M_*(< r_{500})/M_{500}$ at $z = 0$. A model varying f_* with mass in this manner is shown in Fig. 1 as dot-dashed lines. As one would expect, this decreases the gas fraction more in lower mass halos; it also changes the slope of the $M - T_X$ relation slightly.

The slopes of the $M - T_X$ and $M - Y_X$ relations will clearly depend on how strongly M_* varies with halo mass. Recently Gonzalez et al. (2007) found a much steeper relation in a sample of 23 clusters: $M_*(< r_{500})/M_{500} \propto M_{500}^{-0.64}$. A model where f_* follows this relation is shown as long-dashed lines in Fig. 1. The effect is quite dramatic in low mass clusters because so much gas is converted into stars ($\sim 50\%$ or more), and the resulting T_X and gas fractions tend to overshoot the observed trends at low masses. If we start with the Lin et al. (2003) and vary the slope, searching for a best-fit model as described in Sec. 2.2, we find an exponent of $\alpha_* = 0.49$ yields a cluster sample with $M - T_X$ and $M - Y_X$ relations quite close to those observed; this model is shown as solid lines in Fig. 1. We will refer to this choice of parameters ($\epsilon_D = 0.05$, $f_* \propto M_{500}^{-0.49}$, $\epsilon_F = 0$, $\delta_{rel} = 0$) as our “SF-only” model.

The second effect which can break the scale-free nature of the models is additional energy injection, e.g. from SNe or AGN. We will assume such feedback is proportional to the number of stars formed, M_F (see Appendix A). As an estimate of the amount of energy under consideration, for $f_*=9\%$ and feedback energy $10^{-5} M_F c^2$, the energy added amounts to 0.8 keV per particle initially inside r_{vir} . Core collapse SNe could only add 0.4 keV/particle (assuming the model in Appendix A and 10^{51} erg per event), so in this case there must be some additional source such as AGN energy from accreting black holes. If the mass in black holes is $10^{-3} M_*$, and 2% of the rest mass energy of the accreted material is converted into

thermal energy (Allen et al. 2006), then an additional 1.0 keV/particle could be added to the gas.

Fig. 2 shows the effect of adding feedback, starting with $\epsilon_D = 0.05$ and $f_* = 9\%$. The long-dashed lines are for an extreme model with $\epsilon_F = 2.0 \times 10^{-5}$. For the most massive halos, the feedback energy is not significant compared to the binding energy of the cluster; hence there is little change evident. For less massive clusters, the added energy is enough to cause the gas to expand, lowering the gas fraction considerably. The $M - T_X$ relation becomes less steep as well, as lower mass halos become hotter; the $M - Y_X$ relation is thus less steep also, though in this example the change is so large as to be incompatible with observations.

Varying the amount of feedback, the best-fit search yields a more moderate level of $1.2 \times 10^{-5} M_F c^2$, shown as solid lines in Fig. 2. We will call this ($\epsilon_D = 0.05, f_* = 0.09, \epsilon_F = 1.2 \times 10^{-5}, \delta_{rel} = 0$) the “Feedback” model. Like the SF-only model, this reproduces quite well the observed $M - T_X$ and $M - Y_X$ relations. The efficiency 1.2×10^{-5} is smaller than the equivalent number used in Paper II for several reasons. Part of the difference is merely bookkeeping: Paper II did not consider mass loss from stars, and expressed feedback as being proportional to M_* , while here we instead use the larger mass M_F . More substantially, Paper II did not include the $\epsilon_D |E_D|$ term, instead effectively considering it as part of the feedback. Finally, here the gas surface pressure is calculated over a smaller radial buffer zone than in Paper II, which leads to a slightly lower gas fraction initially.

Figs. 1 and 2 show that there is a degeneracy between steepening the star formation efficiency as a function of halo mass and increasing the amount of feedback per unit stellar mass. This is shown schematically in Fig. 3. We have found two models which both reproduce the X-ray data reasonably well: the SF-only model, which varies star formation efficiency as $f_* \propto M_{500}^{-0.49}$ (steeper than the values found by Lin et al. (2003) or Giodini et al. (2009), but less steep than Gonzalez et al. (2007)), and the Feedback model, which instead has constant $f_* = 9\%$ and adds feedback $1.2 \times 10^{-5} M_F c^2$. A third option is of course some combination of these two. Since a stellar mass fraction independent of mass does appear to be contradicted by observations, we will adopt the star formation efficiency as given by Lin et al. (2003) and vary ϵ_F to find the best-fit model. This results in a lower level of feedback, $\epsilon_F = 4 \times 10^{-6}$. We will call this our “Standard” model ($\epsilon_D = 0.05, f_* \propto M_{500}^{-0.26}, \epsilon_F = 4 \times 10^{-6}, \delta_{rel} = 0$), which we will use for the rest of the paper. Fig. 4 shows the $M - T_X$ and $M - Y_X$ relations for this third model. This choice of parameters yields a population with thermal energy as a function of mass quite close to that seen by Vikhlinin et al. (2009) and Sun et al. (2009). However, keep in mind that there will be a range of models around this one which will fit the X-ray data equally well— it would be difficult to distinguish between these three models based solely on the gas profiles. The shaded region in Fig. 3 gives a rough idea of the

acceptable range of α_* and ϵ_F .

There is one further physical effect to be considered, namely nonthermal pressure support, e.g. from cosmic rays or magnetic fields (e.g. Pfrommer et al. 2007). We will conclude this section by considering how a moderate level of nonthermal support affects our model. If in fact $\delta_{rel} = 0.10$, then the M_{500} derived from X-rays are too low, because they are derived by assuming hydrostatic equilibrium. Fig. 5 shows our Standard model, after adjusting masses in the observational points by 10% to account for this; in this situation the model now has too high T_X and f_g at a given M_{500} . Adding $\delta_{rel} = 0.10$ to this model means that the gas requires less thermal pressure to maintain hydrostatic equilibrium, so the solution to Eqns. 5 and 6 yields gas which is cooler and correspondingly denser. This is shown as dashed lines in Fig. 5; the model is now too cold, and the gas fraction even higher. Comparing to Fig. 1, it can be seen that increasing δ_{rel} has the opposite effects of increasing ϵ_D . If we take the $\delta_{rel} = 0.10$ model and allow the dynamical energy input to vary, the best-fit result has $\epsilon_D = 0.10$, shown as solid lines in Fig. 5. This puts our predicted clusters back into agreement with the (adjusted) observations, at the same level as the Standard model. We will call this set of parameters ($\epsilon_D = 0.10, f_* \propto M_{500}^{-0.26}, \epsilon_F = 4 \times 10^{-6}, \delta_{rel} = 0.10$) the “ $\delta_{rel} = 10\%$ ” model.

Increasing ϵ_D in this way assumes that non-radiative hydrodynamic simulations are missing some processes which transfer energy to gas during cluster formation. This certainly could be the case. For example, the dynamical friction experienced by the stars assembling into a cD galaxy would add significant amounts of energy to the ICM (El-Zant et al. 2004; Kim 2007; Conroy & Ostriker 2008).

4. Radial Profiles

Having fixed on a Standard model, in this section we will examine how well it matches observations at other radii than r_{500} .

Given that our DM halos have the standard density profile, the $M_{2500} - T_X$ relation of our model should also agree with observations. Fitting all halos with $kT_X > 1\text{keV}$, the best fit power law relation gives a normalization of $M_{2500}E(z) = 1.25 \times 10^{14} h^{-1} M_\odot$ at $kT_X = 5\text{keV}$. This agrees well with observed X-ray samples, using masses derived from either weak lensing (Hoekstra 2007) or X-rays (Arnaud et al. 2005; Vikhlinin et al. 2006).

The Standard model also has an X-ray luminosity in good agreement with the observations of Vikhlinin et al. (2009), unlike the Zero model which is a factor of 2-3 more luminous. This is hardly surprising, since we calibrated the model in part on this data. Above $10^{14} M_\odot$,

the predicted $L_X \propto M_{500}^{1.77}$, but below this the relation is much steeper, approaching $M_{500}^{2.83}$. Vikhlinin et al. (2009) find the observed scatter at a given mass is $\approx \pm 48\%$, while the model scatter is roughly half of this. There are many processes occurring in the cores of clusters which could significantly alter L_X not included in our model, which would increase the scatter and somewhat alter the mass dependence.

A fundamental property of the gas is its entropy, usually defined in cluster studies as $K \equiv kT/n_e^{2/3}$, where n_e is the electron number density. Based on Chandra observations of nearby relaxed clusters, Nagai et al. (2007) determined how entropy varies with cluster temperature at several characteristic radii, including r_{500} , r_{1000} , and r_{2500} . Their best-fit power-law approximations of these data are shown in Fig. 6 as dashed lines, which shows the entropy at these three radii as a function of T_X . The Zero model gives too low entropy values at all radii; true clusters have shallower entropy profiles than the scale-free model predicts. Once star formation and feedback are included, however, there is much improved agreement with observed clusters; the main disagreement is at r_{500} , where the model is roughly 10% too high. Sun et al. (2009) also determined $K - T_X$ relations at these radii, using Chandra archival data and including many lower temperature groups. For $T_X > 2\text{keV}$, the median value from the model clusters is within 10% of their power-law fits at r_{500} and r_{1000} . At r_{2500} the model is lower than the Sun et al. (2009) relation by roughly 15%, for all but the most massive clusters. Our model does not consider the history of cluster formation, nor the fact that the nonadiabatic processes which can alter the entropy will likely be more pronounced in the core.

Afshordi et al. (2007) assembled a heterogeneous catalog of 193 X-ray clusters and then examined *WMAP* data to derive a mean pressure profile using the SZ effect. This profile is shown as points with error bars in Fig. 7; the pressure is normalized to the critical density times the global cluster T_X . For comparison, we computed the mean profile of the 284 clusters from our Standard sample with $kT_X > 3\text{keV}$. This is shown as solid line in Fig. 7; the mean profile of the same halos without star formation or energy input is shown as a dotted line. To scale the radius, r_{200} is estimated from kT_X (as in Eqn. 1 of Afshordi et al. 2007), though using the radius measured directly from the DM distribution gives the same results. Outside of $0.5r_{200}$, changes to the gas energy show little effect on the mean profile. At smaller radii, star formation and feedback reduce the density more than they affect the temperature profile, thus lowering the pressure profile in the core. This gives better agreement with the Afshordi et al. (2007) profile, though it is still higher. One source of this disagreement is that they assumed $\rho T \propto r^{-2}$ inside $0.25r_{200}$ when constraining their profile, while our model is shallower than this; had they assumed a similarly shallow inner profile, this point would have been higher. Note also the redshift and temperature distributions of the model and observed samples are quite different.

Bonamente et al. (2008) present a joint SZ and X-ray analysis of 38 clusters; here we will compare to their low-redshift sample of 19 clusters in the range $0.14 \leq z \leq 0.30$. For our Standard sample with $z \leq 0.2$ we calculated the integrated Compton y-parameter, Y (Eqn. 6 of Bonamente et al. 2008), out to projected R_{2500} ; this is shown in Fig. 8. Most of our sample is at lower gas masses than the clusters used by Bonamente et al. (2008), but where the two samples overlap the agreement is good. The best fit power-law found by Bonamente et al. (2008), with slope 1.60, is shown as a dashed line in Fig. 8. A power-law fit to our model halos with $M_g(< r_{2500}) \geq 8 \times 10^{12} h^{-1} M_\odot$ yields a slope of 1.61. Also shown as a dotted line is the Zero model. The effect of increasing the gas energy is to cause gas to expand and reduce the gas mass; however, this does not change the integrated pressure profile much, since the gas in the center must still hold up all the gas above it. This effect is larger for smaller mass halos, making the $Y - M_g$ relation less steep.

In Sec. 3 we found several different models which, given the degeneracy among input parameters, gave similar results. Since one goal of this is to provide a means of predicting the SZ signal from clusters, it is useful to compare these models. Fig. 9 shows the fractional difference in the Y value from the Standard model, as a function of $M_g(< r_{2500})$, for the SF-only, Feedback, and $\delta_{rel} = 10\%$ models. The median SZ signal is within 10% of the Standard model in each case, and they are all roughly a factor of 2 higher than the Zero model, which does not include star formation and energy injection. This highlights the importance of normalizing to X-ray data when modeling the SZ signal.

5. Summary and Discussion

In this paper we have described an improved method for calculating the gas distribution in a DM potential well, constraining the model to match the observed X-ray gas fractions; then we made further comparisons with X-ray and SZ observations in order to check, where possible, our conclusions. Extracting the greatest return from upcoming cluster surveys will require understanding the state of the intracluster gas. It is encouraging that the simple model presented here can so well reproduce observed profiles and trends with cluster mass. With this model the following main points have demonstrated:

- Simulations show that during mergers the energy of the DM component will be tapped to provide shock heating to the gas. Transferring $\sim 5\%$ of the binding energy of the DM to the gas results in gas fractions at large radii which are in good agreement with non-radiative hydrodynamical simulations.
- Breaking the scale-free nature of the model to bring it into accord with observed scalings requires either varying the efficiency of star formation with cluster mass or increasing the

specific energy of the gas by an amount that is not proportional to the cluster binding energy (e.g. by being proportional to the stellar mass), or both.

- Without including feedback energy, varying the efficiency of star formation as $f_* \propto M_{500}^{-0.49}$ reproduces observed $M - T_X$ and $M - Y_X$ relations. This is steeper than found by Lin et al. (2003) and Giodini et al. (2009), but less steep than found by Gonzalez et al. (2007). A relation as steep as $f_* \propto M_{500}^{-0.64}$, as seen by the latter, would leave too small gas fractions (and that gas at too high temperatures) in less massive clusters; however, the difference is less than two sigma. Also, keep in mind that what is measured is the stellar fraction inside r_{500} , whereas f_* in our model is the fraction inside r_{vir} ; the two need not be identical. We are assuming that stars have the same radial distribution as DM, but if stars are instead more centrally located, this would change our predicted relation. Gonzalez et al. (2007) selected for clusters with a dominant central galaxy, and for the least massive clusters r_{500} is in the outskirts of this galaxy. Because a central dominant galaxy takes up a larger fraction of the stellar mass in smaller clusters, one could argue that the stellar fraction inside r_{500} changes more rapidly with cluster mass than does the fraction inside r_{vir} , i.e. $M_*(< r_{500})$ should vary with halo mass at a larger rate than f_* .
- A model with M_*/M_{500} independent of cluster mass but including feedback energy proportional to the mass of formed stars can also reproduce the observed $M - T_X$ and $M - Y_X$. However, this requires adding roughly one keV per particle initially inside r_{vir} . This might be possible if the output from accreting black holes is converted to thermal energy with high enough efficiency (~ 0.02).
- The most likely possibility is that both star formation and feedback are at work. Assuming $f_* \propto M^{-0.26}$ (as in Lin et al. 2003) and including a lower feedback level of $4 \times 10^{-6} M_{FC}^2$ also yields the proper scalings. Assuming the mass in black holes is $10^{-3} M_*$, this energy is 6.5×10^{-3} of their rest mass (or 0.33 keV per particle; note this does not take into account the feedback supplied by supernovae). This model was compared to further observations in Sec. 4, but the other two possibilities discussed here behave in quite a similar fashion.
- Including nonthermal pressure results in a cooler, denser gas distribution. To bring such a model back into agreement with X-ray observations requires increased energy input. Once this is done, the pressure or entropy for a given T_X is quite similar to models with $\delta_{rel} = 0$, although of course the $M - T_X$ relation is different.

A couple caveats are in order. We start with halos drawn from a DM-only simulation; adding baryons to such a simulation may change the properties of the halo population (Stanek et al. 2009). Also, we have neglected many pertinent physical processes, such as cooling in the core (note our definition of cluster temperature excludes the core). Because of this, the model halo population likely has too low a scatter at a given mass. This is exacerbated by the tight relation we assume between halo mass and star formation plus feedback.

For example, if we allowed for a variation in f_* at a given halo mass, clusters with higher M_* would have higher temperatures and lower gas fractions, and thus lower X-ray luminosities. This would explain why catalogs of optically selected clusters tend to be underluminous in X-rays at the same mass (Rykoff et al. 2008).

For most halos in our standard model, the gas initially assumed to be inside r_{vir} has expanded outwards. For hotter ($kT > 3\text{keV}$) clusters only, the mean final radius r_f is 1.23 ± 0.13 (one sigma); for all clusters the mean r_f is 1.47 ± 0.30 . A result of this is that for the most massive clusters the baryon fraction inside r_{vir} is roughly 90% of the cosmic mean, $f_c \equiv \Omega_b/\Omega_m$. Fig. 10 shows the the baryon fraction inside r_{500} as a function of cluster mass for differing input parameters. The models shown have similar gas fractions (by design), but varying stellar mass fractions. This results in differing total baryon fractions at lower masses (though, as pointed out above, this may change if stars are more centrally concentrated than DM). In every case, however, the baryon fraction inside r_{500} tops out near $0.8f_c$ at the highest cluster masses. Our sample contains four halos with virial masses above $10^{15}h^{-1}M_\odot$; their gas fractions within r_{200} vary from $0.71f_c$ to $0.82f_c$, with a mean of $0.78f_c$. This agrees well with the detailed multiwavelength analysis of four massive clusters by Umetsu et al. (2008). Gonzalez et al. (2007) also found baryon fractions inside r_{500} near $0.8f_c$ at high masses. As this work was nearing completion, Giodini et al. (2009) published a new determination of the baryon fraction (not including intra-cluster light) as a function of cluster mass. Our Standard model is in good agreement with their result, shown as a dotted line in Fig. 10.

The “missing” gas in this model is distributed in the outskirts of clusters. There it would be difficult to observe directly, being at low temperatures and densities. However, Prokhorov (2008) has predicted in this case there would be emission in the extreme ultraviolet from these outer shells. Alternatively, as this gas is associated with clusters, its kinetic SZ signature should be correlated with the cluster velocity field (Ho et al. 2009; Hernandez-Monteagudo & Ho 2009).

Computer simulations and analysis were supported by the National Science Foundation through TeraGrid resources provided by Pittsburgh Supercomputing Center and the National Center for Supercomputing Applications under grant AST070015; computations were also performed at the TIGRESS high performance computer center at Princeton University, which is jointly supported by the Princeton Institute for Computational Science and Engineering and the Princeton University Office of Information Technology. PB was partially supported by NSF Grant 0707731.

A. Star formation, gas recycling, and metal formation

We will follow the “fossil” model of Nagamine et al. (2006), which matches local stellar populations; this represents a bulge and a disk component with delayed exponentials. Let $M_F(\tau_j, t)$ denote the mass in stars of type j formed by time t , and $F_j = M_F(\tau_j, t_H)$ the total mass of such stars ever formed by a time t_H corresponding to redshift zero, i.e. today. (At this point no allowance is made for mass lost from stars.) For the time evolution of this stellar mass we will adopt

$$M_F(\tau_j, t) = \frac{F_j}{\chi_*(\tau_j, t_H)} \chi_*(\tau_j, t) = \frac{F_j}{\chi_*(\tau_j, t_H)} \left[1 - \left(\frac{t}{\tau_j} + 1 \right) e^{-t/\tau_j} \right] \quad . \quad (\text{A1})$$

This choice means the star formation rate is given by a delayed exponential

$$\dot{M}_F(\tau_j, t) = \frac{F_j}{\chi_*(\tau_j, t_H)} \dot{\chi}_*(\tau_j, t) = \frac{F_j}{\chi_*(\tau_j, t_H)} \frac{1}{\tau_j} \frac{t}{\tau_j} e^{-t/\tau_j} \quad . \quad (\text{A2})$$

Nagamine et al. (2006) found a combination of a bulge population with decay time $\tau_b=1.5$ Gyr and a disk population with $\tau_d=4.5$ Gyr is most consistent with local stellar populations (hence the term fossil). Since stellar populations in clusters are older than average, we will assume 90% of the total stars formed by $z = 0$ are from the bulge component, and the remaining 10% from the younger disk component. The resulting star formation history is shown in Fig. 11; there is little new star formation for $z \lesssim 1$. This figure assumes $M_*/M_g=0.1$ at $z=0$; note that if r_f increases then the amount of gas inside r_{vir} will decrease, changing the final value of this ratio.

The supernova rate also depends upon the delay time distribution. For a burst of star formation at $t=0$, suppose the fraction of SNe of type i occurring by time t is given by $f_{SN}(\tau_i, t) = 1 - e^{-t/\tau_i}$. Then the number of SNe per unit stellar mass per unit time will follow the commonly used distribution (e.g. Strolger et al. 2004; Mannucci et al. 2006)

$$\Phi(\tau_i, t) = \nu_i \dot{f}_{SN}(\tau_i) = \frac{\nu_i}{\tau_i} e^{-t/\tau_i} \quad , \quad (\text{A3})$$

where ν_i is the total number of SNe of type i per unit mass which will ever occur. The SN rate \dot{S} , i.e. the number of SNe per unit time, is then given by

$$\dot{S}(\tau_i, \tau_j, t) = \int_0^t \Phi(\tau_i, t-s) \frac{dM_F(\tau_j, s)}{ds} ds = \frac{F_j}{\chi_*(\tau_j, t_H)} \nu_i \mu_{ij}^2 \left[\dot{f}_{SN}(\tau_i, t) + \dot{\chi}_*(\tau_j, t) \frac{\tau_j}{\tau_i} \left(\frac{1}{\mu_{ij}} - \frac{\tau_j}{t} \right) \right] \quad , \quad (\text{A4})$$

where $\mu_{ij} \equiv \tau_i/(\tau_j - \tau_i)$; we will be assuming $\tau_i \neq \tau_j$ and $\tau_i > 0$ throughout. Finally, the cumulative number of SNe of type i which have occurred by time t is

$$S(\tau_i, \tau_j, t) = \int_0^t \frac{dS(\tau_i, \tau_j, s)}{ds} ds = \frac{F_j}{\chi_*(\tau_j, t_H)} \nu_i \chi(\tau_i, \tau_j, t) \quad , \quad (\text{A5})$$

$$\chi(\tau_i, \tau_j, t) = \mu_{ij}^2 \left[f_{SN}(\tau_i, t) + \frac{1}{\mu_{ij}} \frac{\tau_j}{\tau_i} \chi_*(\tau_j, t) + \frac{\tau_j}{\tau_i} (e^{-t/\tau_j} - 1) \right]. \quad (\text{A6})$$

Thus it only remains to specify ν_i and τ_i for each type of SN.

For core collapse SNe, the delay time is short; we will adopt $\tau_{CC} = 0.01$ Gyr. We will employ a simple IMF with a slope of -0.5 for stellar masses in the range $0.1 - 0.5 M_\odot$ and Salpeter slope -1.35 for $0.5 - 100 M_\odot$ (Baldry & Glazebrook 2003). Assuming all stars in the range $8-50 M_\odot$ end their lives as SNCC, then $\nu_{CC} \approx 9.14 \times 10^{-3}$.

The picture for SNIa is more complicated. There is growing evidence for a prompt SNIa component with a short delay time after star formation (e.g. Della Valle et al. 2005; Mannucci et al. 2005, 2006; Neill et al. 2006; Sullivan et al. 2006; Aubourg et al. 2007, and references therein). On the other hand, much observational evidence points towards much longer delay times of 2-4 Gyr (e.g. Gallagher et al. 2005; Mannucci et al. 2005; Sullivan et al. 2006; Forster & Schawinski 2008, and references therein). Scannapieco & Bildsten (2005) proposed that two evolutionary channels exist, a prompt population that would be proportional to the recent star formation rate, and a tardy one with a much longer delay time that would be proportional to the total stellar mass. Mannucci et al. (2006) found that the data are best matched by equal amounts of SNIa in two populations, one exploding of order 10^8 yr after star formation and the other following an exponential distribution with a decay time of about 3 Gyr. We will follow this model for SNIa, setting a prompt delay time $\tau_p = 0.05$ Gyr for one half, and a tardy $\tau_t = 3$ Gyr for the other half.

Assuming SNIa result from $3-8 M_\odot$ stars, then $\nu_i \approx 0.02754\eta_i$, where η_i is the fraction of the stars in this mass range that go supernova. This fraction is not well constrained; Maoz (2008) examines a number of different estimates of this fraction and finds that they vary from 2% to 40%, but also that $\eta \sim 15\%$ is consistent with all the estimates he considered. Thus we will set $\eta_p = \eta_t = 0.07$, or $\nu_p = \nu_t = 0.00193$, such that there are equal numbers of prompt and tardy SNIa.

In a $(h, \Omega_m, \Lambda) = (0.7, 0.3, 0.7)$ cosmology, this model gives predicted SN rates per unit mass at $z = 0$ of 0.07 SNUM for both SNCC and SNIa. For comparison, Mannucci et al. (2008) find $0.090_{-0.022}^{+0.028}$ and $0.070_{-0.013}^{+0.016}$ SNUM (1σ statistical errors) for SNCC and SNIa, respectively. The predicted rates increase with redshift; the predicted SNIa rate is well within the 1σ (statistical) errors of the rate measured by Sharon et al. (2007) in the redshift range 0.06–0.19, and of the rate measured by Graham et al. (2008) in the range 0.2–1. From the supernova rate one can predict metallicity evolution. Using iron yields per event of $0.077 M_\odot$ for SNCC and $0.749 M_\odot$ for SNIa, the resulting history of iron production is also shown in Fig. 11. Even though there is little star formation at low redshift, iron production continues because of tardy SNIa. Note the predicted metallicity will be proportional to the

amount of star formation; also note that we are assuming spatial homogeneity. Fig. 11 also shows the predicted cumulative ratio of SNIa to SNCC; there are roughly 2.5 SNCC for each SNIa, and SNCC produce $\sim 20\%$ of the iron.

The rate of change in the actual stellar mass is the difference between the star formation rate and the rate at which mass is lost from stars. Codes exist for tracking the mass loss from a stellar population, e.g. the PEGASE.2 code of Fioc & Rocca-Volmerange (1999). We will instead assume that all mass loss, whether from SNe or winds, can be modeled with Eqn. A4. Then the stellar mass M_* follows

$$\dot{M}_*(\tau_j, t) = \dot{M}_F(\tau_j, t) - \sum_i y_i \dot{S}(\tau_i, \tau_j, t) \quad , \quad (\text{A7})$$

where the mass yield y_i is the mean initial mass of stars of type i minus the mean remnant mass, if any. The delay times are adjusted to match the mass loss calculated by the PEGASE.2 code¹ The choices of delay times and yields are summarized in Table 1. We assume SNCC leave behind neutron stars of mass $1.4M_\odot$ and SNIa leave no remnant. Stars larger than $50M_\odot$ are all assumed to collapse to $2M_\odot$ black holes, on the same time scale as SNCC. Stars in the $5 - 8M_\odot$ range which do not go supernova instead remain as $0.55M_\odot$ white dwarfs. The delay time for mass loss from these stars is set to 0.05 Gyr, slower than the prompt SNIa component; this choice is required to match the mass loss on short (< 1 Gyr) time scales. Stars in the $1.1 - 3M_\odot$ range also become white dwarfs, with mass loss on a much longer time scale of 6 Gyr; the lower limit of $1.1M_\odot$ is treated as a free parameter, set to match the mass in white dwarfs at long time scales. Given these parameters, the evolution of the recycled gas fraction and the mass in remnants resulting from a single starburst is shown in Fig. 12; also shown for the same IMF are the predictions of the PEGASE.2 code. Our relatively simple scheme follows the more detailed evolutionary code reasonably well.

REFERENCES

- Afshordi, N., Lin, Y.-T., Nagai, D., & Sanderson, A. J. R. 2007, MNRAS, 378, 293
 Afshordi, N., Lin, Y.-T., & Sanderson, A. J. R. 2005, ApJ, 629, 1
 Allen, S. W., Dunn, R. J. H., Fabian, A. C., Taylor, G. B., & Reynolds, C. S. 2006, MNRAS, 372, 21
 Arnaud, M. & Evrard, A. E. 1999, MNRAS, 305, 631
 Arnaud, M., Pointecouteau, E., & Pratt, G. W. 2005, A&A, 441, 893
 —. 2007, A&A, 474, L37

¹Available at <http://www2.iap.fr/users/fioc/PEGASE.html>

- Ascasibar, Y. & Diego, J. M. 2008, *MNRAS*, 383, 369
- Ascasibar, Y., Yepes, G., Müller, V., & Gottlöber, S. 2003, *MNRAS*, 346, 731
- Aubourg, E., Tojeiro, R., Jimenez, R., Heavens, A. F., Strauss, M. A., & Spergel, D. N. 2007, *ArXiv e-prints*, 707
- Babul, A., Balogh, M. L., Lewis, G. F., & Poole, G. B. 2002, *MNRAS*, 330, 329
- Baldry, I. K. & Glazebrook, K. 2003, *ApJ*, 593, 258
- Balogh, M. L., Babul, A., & Patton, D. R. 1999, *MNRAS*, 307, 463
- Bhattacharya, S., di Matteo, T., & Kosowsky, A. 2008, *MNRAS*, 389, 34
- Bode, P., Ostriker, J. P., Weller, J., & Shaw, L. 2007, *ApJ*, 663, 139
- Böhringer, H. et al. 2007, *A&A*, 469, 363
- Bonamente, M., Joy, M., LaRoque, S. J., Carlstrom, J. E., Nagai, D., & Marrone, D. P. 2008, *ApJ*, 675, 106
- Borgani, S., Diaferio, A., Dolag, K., & Schindler, S. 2008, *Space Science Reviews*, 134, 269
- Borgani, S., Dolag, K., Murante, G., Cheng, L.-M., Springel, V., Diaferio, A., Moscardini, L., Tormen, G., Tornatore, L., & Tozzi, P. 2006, *MNRAS*, 367, 1641
- Bower, R. G., McCarthy, I. G., & Benson, A. J. 2008, *MNRAS*, 390, 1399
- Bryan, G. L. & Norman, M. L. 1998, *ApJ*, 495, 80
- Burenin, R. A., Vikhlinin, A., Hornstrup, A., Ebeling, H., Quintana, H., & Mescheryakov, A. 2007, *ApJS*, 172, 561
- Cen, R. & Ostriker, J. P. 1994, *ApJ*, 429, 4
- Ciotti, L. & Pellegrini, S. 2008, *MNRAS*, 387, 902
- Cohn, J. D. & White, M. 2005, *Astroparticle Physics*, 24, 316
- Conroy, C. & Ostriker, J. P. 2008, *ApJ*, 681, 151
- Crain, R. A., Eke, V. R., Frenk, C. S., Jenkins, A., McCarthy, I. G., Navarro, J. F., & Pearce, F. R. 2007, *MNRAS*, 377, 41
- Dahle, H. 2007, *ArXiv Astrophysics e-prints*
- Davé, R., Oppenheimer, B. D., & Sivanandam, S. 2008, *MNRAS*, 391, 110
- Della Valle, M., Panagia, N., Padovani, P., Cappellaro, E., Mannucci, F., & Turatto, M. 2005, *ApJ*, 629, 750
- Dobbs, M. et al. 2006, *New Astronomy Review*, 50, 960
- Dos Santos, S. & Doré, O. 2002, *A&A*, 383, 450
- Eisenhardt, P. R. M. et al. 2008, *ApJ*, 684, 905
- Eke, V. R., Navarro, J. F., & Frenk, C. S. 1998, *ApJ*, 503, 569
- El-Zant, A. A., Kim, W.-T., & Kamionkowski, M. 2004, *MNRAS*, 354, 169
- Ettori, S., Dolag, K., Borgani, S., & Murante, G. 2006, *MNRAS*, 365, 1021
- Fakhouri, O. & Ma, C.-P. 2008, *MNRAS*, 386, 577
- Finoguenov, A. et al. 2007, *ApJS*, 172, 182
- Fioc, M. & Rocca-Volmerange, B. 1999, *ArXiv Astrophysics e-prints*
- Forster, F. & Schawinski, K. 2008, *ArXiv e-prints*, 804

- Gallagher, J. S., Garnavich, P. M., Berlind, P., Challis, P., Jha, S., & Kirshner, R. P. 2005, *ApJ*, 634, 210
- Giodini, S. et al. 2009, ArXiv e-prints
- Gonzalez, A. H., Zaritsky, D., & Zabludoff, A. I. 2007, *ApJ*, 666, 147
- Gottlöber, S. & Yepes, G. 2007, *ApJ*, 664, 117
- Graham, M. L. et al. 2008, *AJ*, 135, 1343
- Hernandez-Monteagudo, C. & Ho, S. 2009, ArXiv e-prints
- Ho, S., Dedeo, S., & Spergel, D. 2009, ArXiv e-prints
- Hoekstra, H. 2007, *MNRAS*, 379, 317
- Kaiser, N. 1991, *ApJ*, 383, 104
- Kay, S. T., da Silva, A. C., Aghanim, N., Blanchard, A., Liddle, A. R., Puget, J.-L., Sadat, R., & Thomas, P. A. 2007, *MNRAS*, 377, 317
- Kim, W.-T. 2007, *ApJ*, 667, L5
- Koester, B. P. et al. 2007, *ApJ*, 660, 239
- Komatsu, E. et al. 2008, ArXiv e-prints
- Komatsu, E. & Seljak, U. 2001, *MNRAS*, 327, 1353
- Kosowsky, A. 2006, *New Astronomy Review*, 50, 969
- Lapi, A., Cavaliere, A., & Menci, N. 2005, *ApJ*, 619, 60
- Lin, K.-Y. et al. 2008, in *Astronomical Society of the Pacific Conference Series*, Vol. 399, *Astronomical Society of the Pacific Conference Series*, ed. T. Kodama, T. Yamada, & K. Aoki, 384-
- Lin, Y.-T., Mohr, J. J., & Stanford, S. A. 2003, *ApJ*, 591, 749
- Loewenstein, M. 2000, *ApJ*, 532, 17
- Lopes, P. A. A., de Carvalho, R. R., Kohl-Moreira, J. L., & Jones, C. 2009, *MNRAS*, 392, 135
- Malte Schäfer, B. & Bartelmann, M. 2007, *MNRAS*, 377, 253
- Mannucci, F., Della Valle, M., & Panagia, N. 2006, *MNRAS*, 370, 773
- Mannucci, F., Della Valle, M., Panagia, N., Cappellaro, E., Cresci, G., Maiolino, R., Petrosian, A., & Turatto, M. 2005, *A&A*, 433, 807
- Mannucci, F., Maoz, D., Sharon, K., Botticella, M. T., Della Valle, M., Gal-Yam, A., & Panagia, N. 2008, *MNRAS*, 383, 1121
- Maoz, D. 2008, *MNRAS*, 384, 267
- McCarthy, I. G., Bower, R. G., Balogh, M. L., Voit, G. M., Pearce, F. R., Theuns, T., Babul, A., Lacey, C. G., & Frenk, C. S. 2007, *MNRAS*, 376, 497
- Mewe, R., Gronenschild, E. H. B. M., & van den Oord, G. H. J. 1985, *A&AS*, 62, 197
- Moodley, K., Warne, R., Goheer, N., & Trac, H. 2008, ArXiv e-prints
- Muanwong, O., Kay, S. T., & Thomas, P. A. 2006, *ApJ*, 649, 640
- Muchovej, S. et al. 2007, *ApJ*, 663, 708
- Nagai, D., Kravtsov, A. V., & Vikhlinin, A. 2007, *ApJ*, 668, 1
- Nagamine, K., Ostriker, J. P., Fukugita, M., & Cen, R. 2006, *ApJ*, 653, 881

- Neill, J. D. et al. 2006, *AJ*, 132, 1126
- Ostriker, J. P., Bode, P., & Babul, A. 2005, *ApJ*, 634, 964
- Pacaud, F. et al. 2007, *MNRAS*, 382, 1289
- Pfrommer, C., Enßlin, T. A., Springel, V., Jubelgas, M., & Dolag, K. 2007, *MNRAS*, 378, 385
- Pratt, G. W., Croston, J. H., Arnaud, M., & Boehringer, H. 2008, *ArXiv e-prints*
- Prokhorov, D. A. 2008, *A&A*, 492, 651
- Puchwein, E., Sijacki, D., & Springel, V. 2008, *ApJ*, 687, L53
- Rykoff, E. S., McKay, T. A., Becker, M. R., Evrard, A., Johnston, D. E., Koester, B. P., Rozo, E., Sheldon, E. S., & Wechsler, R. H. 2008, *ApJ*, 675, 1106
- Scannapieco, E. & Bildsten, L. 2005, *ApJ*, 629, L85
- Sehgal, N., Trac, H., Huffenberger, K., & Bode, P. 2007, *ApJ*, 664, 149
- Sharon, K., Gal-Yam, A., Maoz, D., Filippenko, A. V., & Guhathakurta, P. 2007, *ApJ*, 660, 1165
- Shimizu, M., Kitayama, T., Sasaki, S., & Suto, Y. 2004, *PASJ*, 56, 1
- Short, C. J. & Thomas, P. A. 2008, *ArXiv e-prints*
- Sijacki, D., Springel, V., di Matteo, T., & Hernquist, L. 2007, *MNRAS*, 380, 877
- Solanes, J. M., Manrique, A., González-Casado, G., & Salvador-Solé, E. 2005, *ApJ*, 628, 45
- Stanek, R., Rudd, D., & Evrard, A. E. 2009, *MNRAS*, L172+
- Staniszewski, Z. et al. 2008, *ArXiv e-prints*
- Strolger, L.-G. et al. 2004, *ApJ*, 613, 200
- Sullivan, M. et al. 2006, *ApJ*, 648, 868
- Sun, M., Voit, G. M., Donahue, M., Jones, C., Forman, W., & Vikhlinin, A. 2009, *ApJ*, 693, 1142
- Suto, Y., Sasaki, S., & Makino, N. 1998, *ApJ*, 509, 544
- Tozzi, P. & Norman, C. 2001, *ApJ*, 546, 63
- Umetsu, K. 2008, *ArXiv e-prints*
- Vikhlinin, A. 2006, *ApJ*, 640, 710
- Vikhlinin, A., Burenin, R. A., Ebeling, H., Forman, W. R., Hornstrup, A., Jones, C., Kravtsov, A. V., Murray, S. S., Nagai, D., Quintana, H., & Voevodkin, A. 2009, *ApJ*, 692, 1033
- Vikhlinin, A., Kravtsov, A., Forman, W., Jones, C., Markevitch, M., Murray, S. S., & Van Speybroeck, L. 2006, *ApJ*, 640, 691
- Voit, G. M. & Bryan, G. L. 2001, *ApJ*, 551, L139
- Voit, G. M., Bryan, G. L., Balogh, M. L., & Bower, R. G. 2002, *ApJ*, 576, 601
- Wu, K. K. S., Fabian, A. C., & Nulsen, P. E. J. 2000, *MNRAS*, 318, 889
- Yee, H. K. C., Gladders, M. D., Gilbank, D. G., Majumdar, S., Hoekstra, H., & Ellingson, E. 2007, in *Astronomical Society of the Pacific Conference Series*, Vol. 379, *Cosmic Frontiers*, ed. N. Metcalfe & T. Shanks, 103-

This preprint was prepared with the AAS L^AT_EX macros v5.2.

Table 1. Decay times and yields

mass range	mean mass	remnant type	remnant mass	η_i (fraction)	ν_i (M_{\odot}^{-1})	τ_i (Gyr)
50-100	68.4	BH	2.0	1	5.11×10^{-4}	0.01
8-50	16.0	SNCC+NS	1.4	1	9.14×10^{-3}	0.01
3-8	4.58	prompt IA	0	0.07	1.93×10^{-3}	0.05
3-8	4.58	tardy IA	0	0.07	1.93×10^{-3}	3.01
3-8	4.58	WD	0.55	0.92	0.0253	0.5
1.1-3	1.69	WD	0.55	1	0.1078	6.0

Note. — Masses in M_{\odot} .

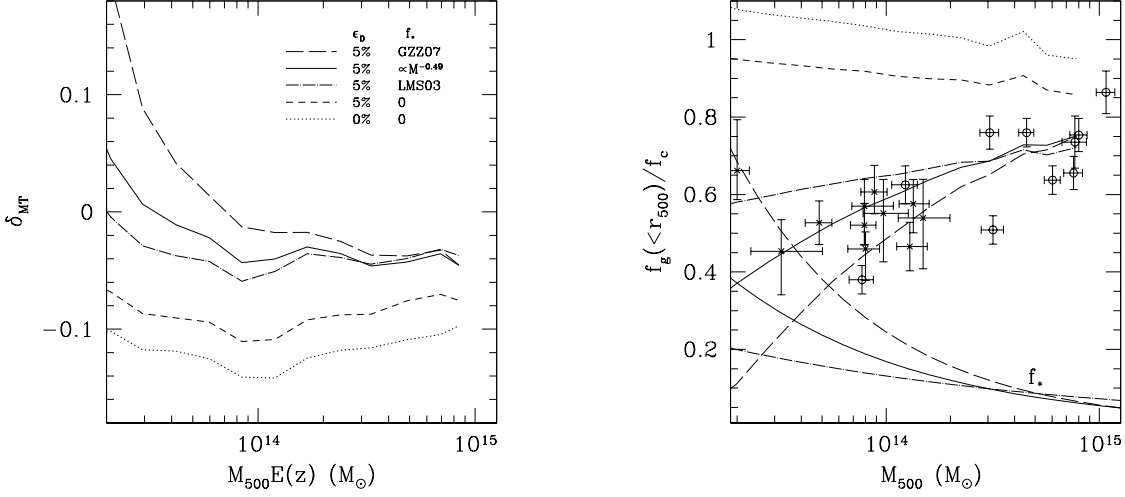


Fig. 1.— Effects of varying star formation. *a*) Fractional difference from the observed mass-temperature relation of Vikhlinin et al. (2009). *b*) Stellar (thinner lines) and gas (thicker lines) fractions, normalized to the cosmic average. Shown are models with: no star formation and $\epsilon_D = 0$ or 0.05 (dotted and short-dashed lines, respectively); also $\epsilon_D = 0.05$ and $f_* \propto M^{-0.26}$ (as in Lin et al. 2003), $f_* \propto M^{-0.49}$, and $f_* \propto M^{-0.64}$ (as in Gonzalez et al. 2007) (dot-dashed, solid, and long-dashed lines). Data points are from Vikhlinin et al. (2006, circles) and Sun et al. (2009, crosses).

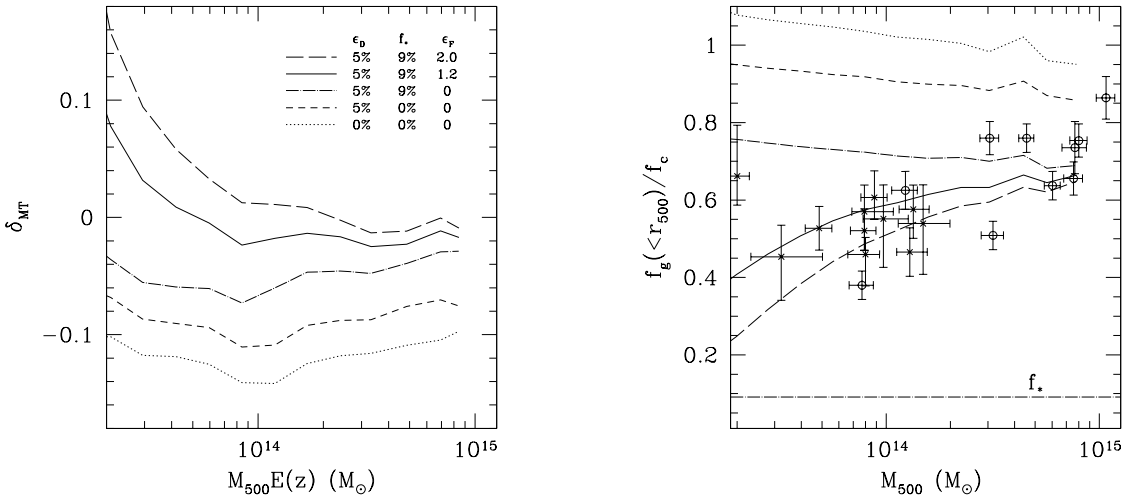


Fig. 2.— Effects of varying feedback. As in Fig.1, showing models with: no star formation and $\epsilon_D = 0$ or 0.05 (dotted and short-dashed lines, respectively); also $\epsilon_D = 0.05$ plus fraction $f_* = 9\%$ of gas converted to stars, with feedback energies of 0, 1.2, and $2.0 \times 10^{-5} M_{FC}^2$ (dot-long dashed, solid, and long-dashed lines).

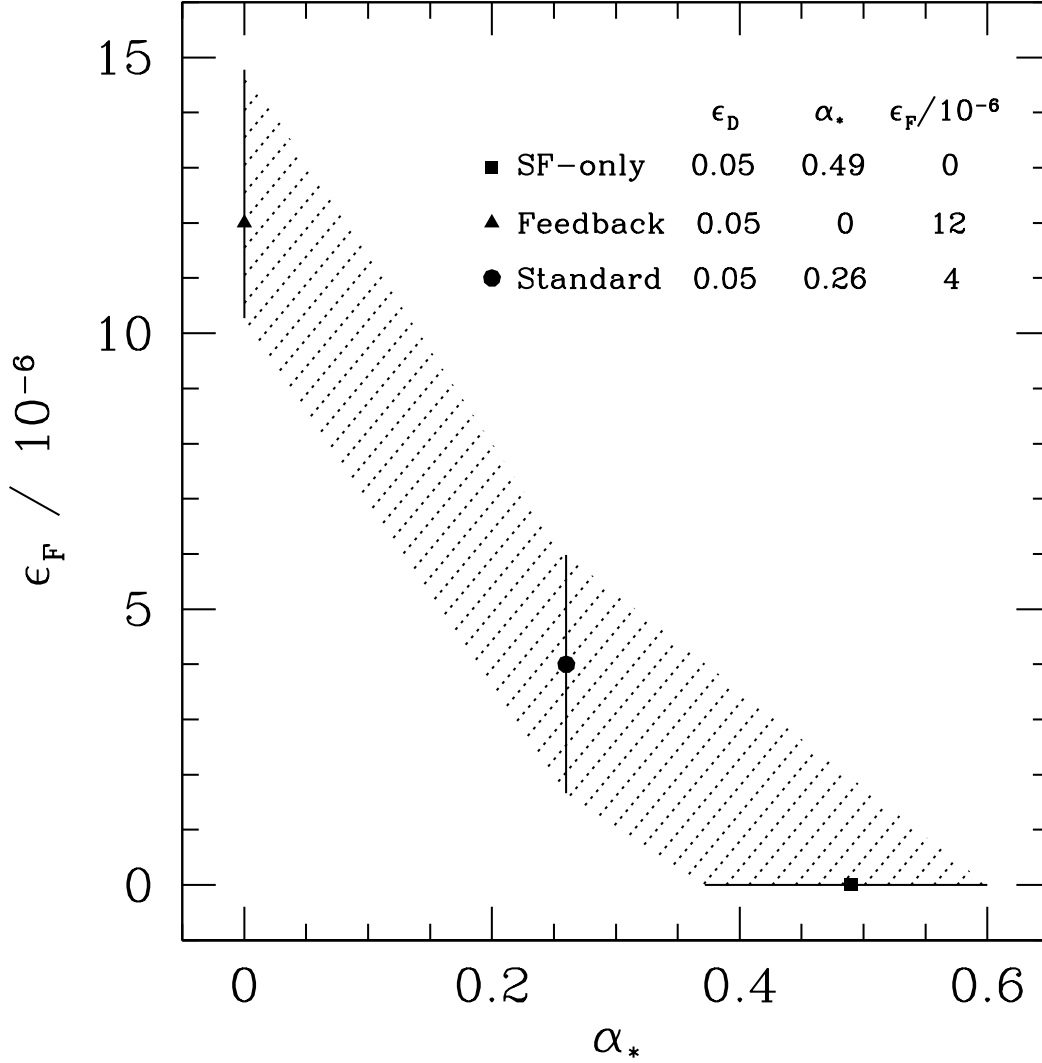


Fig. 3.— Schematic depiction of the degeneracy between varying star formation efficiency $f_* \propto M_{500}^{-\alpha_*}$ and feedback energy $\epsilon_F M_F c^2$. Symbols show three models based on different assumed f_* , as marked. The shaded region denotes a constant $\Delta\chi^2$ from the Standard model, corresponding to a 99% confidence interval for two degrees of freedom (this is only approximate, as we have not minimized over other input parameters).

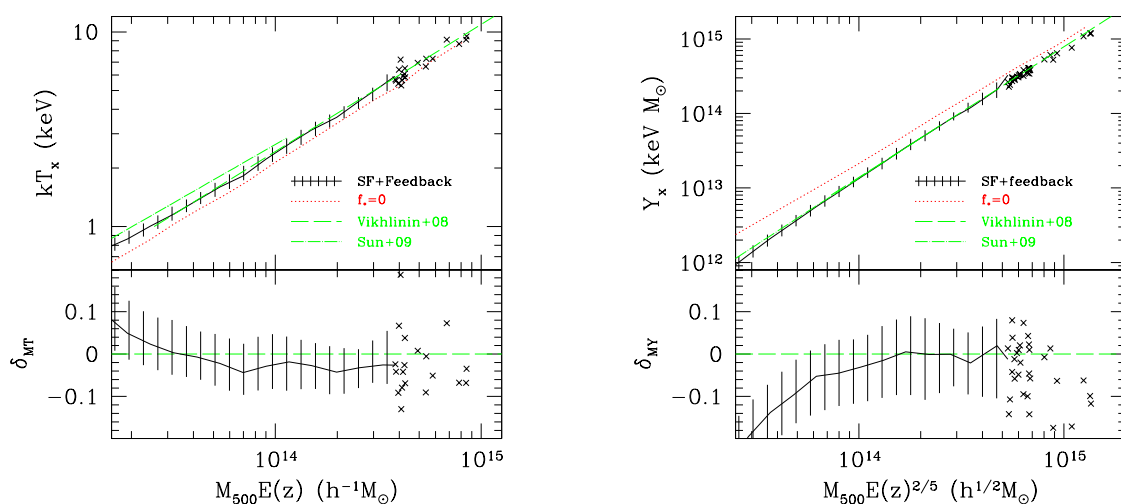


Fig. 4.— Mass-temperature and mass- Y_X relations for the Standard model with $\epsilon_D = 0.05$, f_* as in Lin et al. (2003), and $\epsilon_F = 4 \times 10^{-6}$. Solid lines are the median values, and hash marks denote the region enclosing 68% of the halos. At the high mass end individual halos are shown as \times 's. Dotted lines give the median for the Zero model (no star formation or feedback). Straight lines are the observed best-fit power laws: dashed from Vikhlinin et al. (2009) and dot-dashed from Sun et al. (2009). Lower panels show the fractional difference from the Vikhlinin et al. (2009) relations.

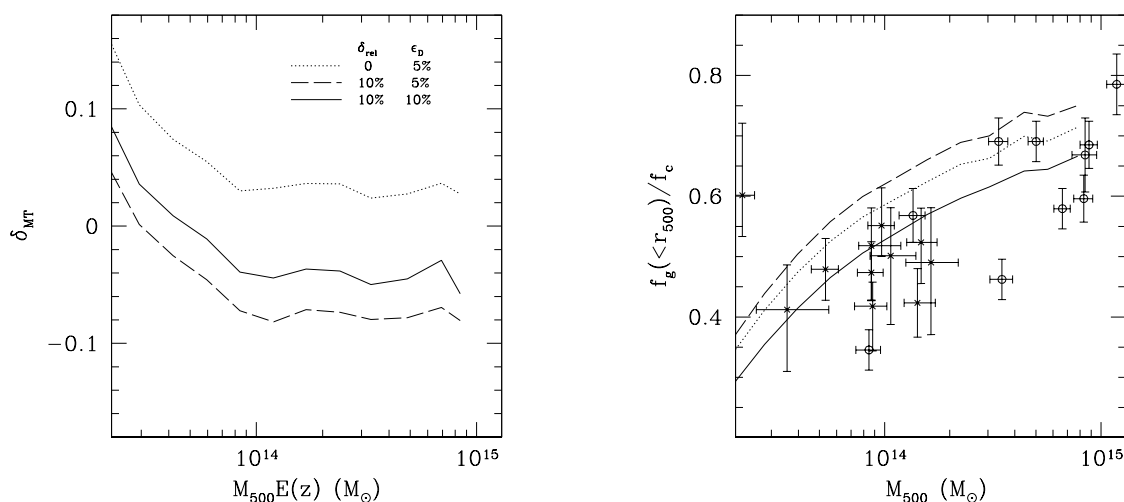


Fig. 5.— Effects of nonthermal pressure. As in Fig.1, but with observational data adjusted to assume a 10% underestimate of cluster mass. Shown are: the Standard model (dotted lines), after including $\delta_{rel} = 0.10$ (dashed lines), and also doubling ϵ_D (solid lines).

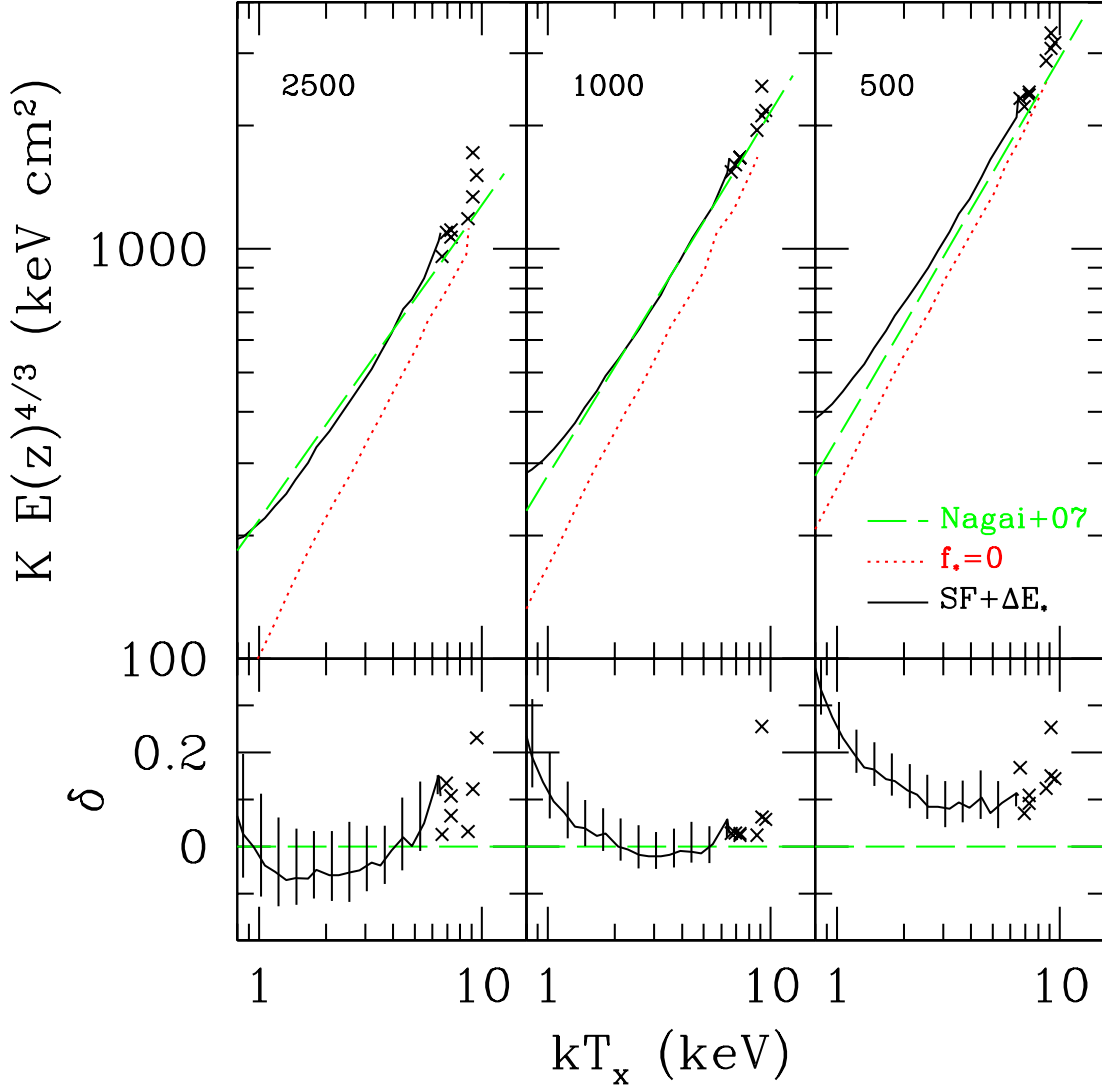


Fig. 6.— Entropy as a function of temperature, at r_{2500} , r_{1000} , and r_{500} . Straight dashed lines are the observed best-fit power laws of Nagai et al. (2007). Solid lines are the median values for the Standard model, dotted lines for the Zero model. For the former, clusters at high T_x are shown as individual points. Lower panels shows the fractional difference of the model from the Nagai et al. (2007) relations.

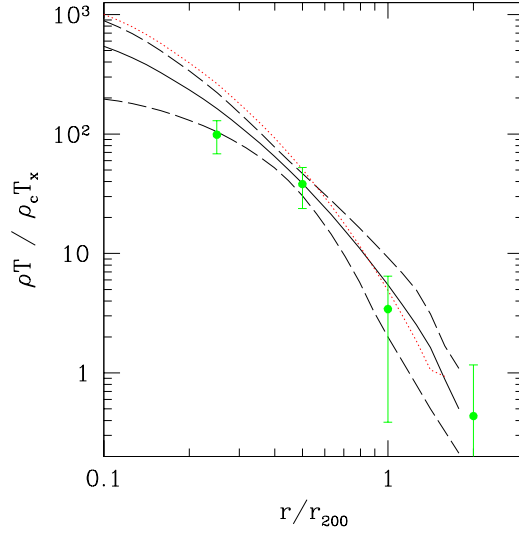


Fig. 7.— The SZ profile as a function of radius. Solid line is the mean profile for all $kT_x > 3\text{keV}$ clusters; dashed lines show two standard deviations. The dotted shows the mean profile for the Zero model. Points with error bars are the mean profile found from WMAP data by Afshordi et al. (2007).

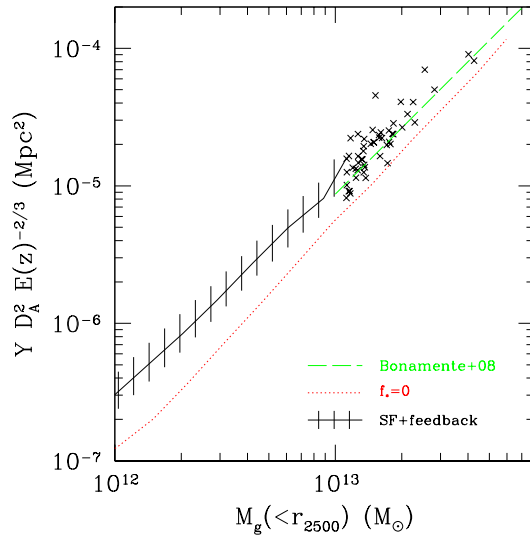


Fig. 8.— The SZ signal as a function of gas mass at overdensity 2500. The solid line is the median values, with hash marks denoting the region enclosing 68% of the halos; at the high mass end individual halos are shown as \times 's. The dotted line is the median for a model with no star formation or feedback. The long-dashed line is the observed relation of Bonamente et al. (2008).

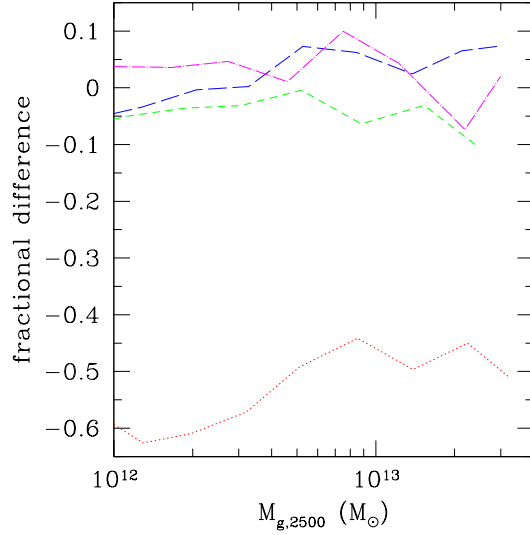


Fig. 9.— Fractional difference of the SZ signal Y from the Standard model. Shown are the Zero (dotted line), SF-only (short-dashed), Feedback (long-dashed), and $\delta_{rel} = 10\%$ (dot-dashed) models.

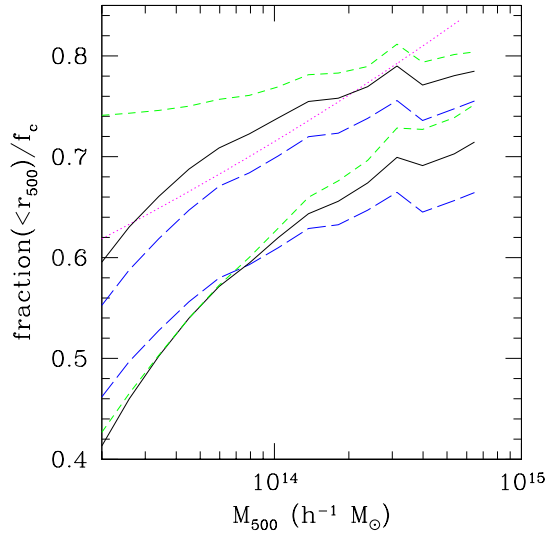


Fig. 10.— Baryon fraction inside r_{500} as a function of mass. The lower set of lines represents gas fraction, and the upper set total baryon fraction. Shown are the Standard (solid lines), SF-only (short-dashed), and Feedback (long-dashed) models. The dotted line is the baryon fraction (not including intra-cluster light) determined by Giodini et al. (2009).

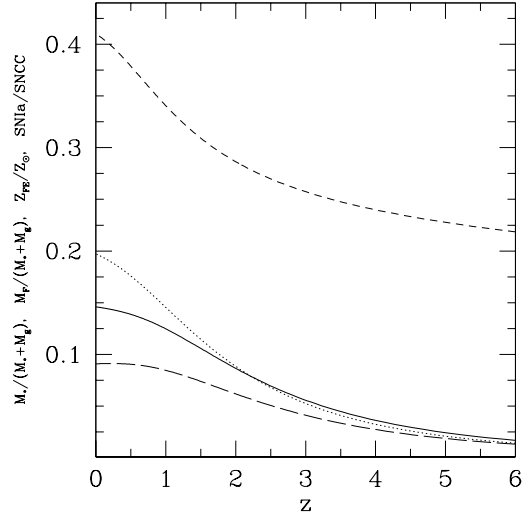


Fig. 11.— Star formation history as a function of redshift. *Long dashed*: mass in stars, as a fraction of all baryons. *Solid*: total mass of stars formed. *Dotted*: metallicity with respect to solar. *Short dashed*: the ratio of SNIa to SNCC. All quantities are measured inside r_f , and assume the redshift zero star/gas ratio is $M_*/M_g=0.10$.

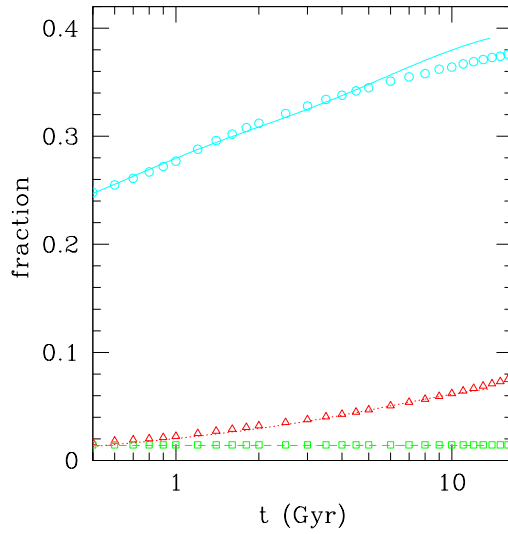


Fig. 12.— Fraction of gas recycled and locked up in remnants as a function of time for a single starburst at $t = 0$. From top to bottom, the lines are fraction of recycled gas (solid), in white dwarfs (dotted), and in black holes or neutron stars (dashed). For comparison, the same quantities as predicted by the PEGASE.2 code (Fioc & Rocca-Volmerange 1999) are shown as circles, triangles, and squares, respectively.